Scaling of computational order parameters in Rydberg-atom graph states

Zhangjie Qin and V. W. Scarola[*]

Department of Physics, Virginia Tech, Blacksburg, Virginia 24061, USA

Graph states are computationally powerful quantum states with many applications, including use as resource states for measurement-based quantum computing (MBQC). We demonstrate construction of graph states on a Rydberg atom quantum analog simulator. We show how an always-on interaction can be used to simultaneously entangle all Rydberg atoms into a graph state. We construct and implement many-body computational order parameters for graph states using nonlocal measurement-based logic operations in the Clifford group. The order parameters measure the efficacy of entanglement to allow MBQC on graph states of any size. We parametrize finite-size scaling of these order parameters. Our results define a route to efficiently test computational power in quantum devices.

I. INTRODUCTION

Graph states are useful quantum many-body spin wave functions that are straightforward to construct [1]. Consider a collection of spins defining graph vertices such that each spin is oriented along the positive-x direction. Application of two-spin entangling operations, e.g., a controlled-Z (CZ) operation between spins, establishes the graph edges. The resulting many-body states have applications in metrology [2,3], they help speed up variational solvers [4], they possess [5–13] symmetry-protected topological order [14], and they are useful in characterizing topological stabilizer quantum error correction codes [15,16]. Graph states are also measurement-based quantum computing (MBQC) resource states [17–19].

Starting with a graph state, MBQC [17,18] can proceed by preparing input on one side of the graph. Local projective measurements throughout the graph then implement quantum logic operations on the input state. The output is obtained on the opposing side of the graph. It was shown that properly designed sequences of measurements [17,18] on graph states are equivalent to circuit-based quantum algorithms, e.g., quantum simulation subroutines [20].

Fault-tolerant MBQC on a two-dimensional cluster state, an example of a graph state with translational invariance, is possible if the probability of an error in resource state preparation and measurement is kept below the threshold [21]

$$\varepsilon_{\mathrm{T}} = 0.0075. \tag{1}$$

The implementation of MBQC error correction discussed in Ref. [21] requires large cluster states. Experimental methods to efficiently create and characterize large graph states are therefore critical to implementing MBQC.

Characterization of large-scale quantum states such as graph states remains challenging. Conventional order parameters used in solids, e.g., magnetization, are insufficient. Our central aim is to define practical order parameters from the perspective of information theory. We define computational order parameters as the fidelities to implement measurement-based quantum logic operations in the Clifford group. The order parameters define the efficacy to compute with the graph state. The MBQC Clifford operations rely on n measurements on N vertices of a graph state. They can be made global such that $n = N$. Finite-size scaling of these order parameters establishes the domain size over which graph states can effectively be used in MBQC provided we define order parameter thresholds. These order parameters can be used to characterize N-atom graph states with $n = N$ global measurements such that their scaling offers a benchmarking tool.

We consider benchmarking of graph states of neutral atoms in optical tweezer arrays as an application because these systems [22,23] are rapidly scaling up in size [24]. Recent experiments [25] constructed and benchmarked cluster states with atoms in an optical tweezer array operating in a digital mode [23]. Here, pseudospin states were encoded into hyperfine states of Rydberg atoms. Rydberg atoms interact via the van der Waals interaction at long distances [22,23]. To avoid crosstalk induced by long-range tails of the interaction, the atoms were coherently shuttled far from other atoms to entangle them pairwise into a cluster state. The 12-atom cluster state chain was benchmarked by measuring a three-atom stabilizer expectation value [25].

We demonstrate construction and benchmarking of large graph states on a Rydberg atom quantum analog simulator, QuEra's Aquila [26], as depicted in Fig. 1. Aquila operates under the following analog conditions [26]: (1) The locations of up to 256 ^{87}Rb atoms are defined in the plane at the start of a run and held in place with optical tweezers for the entirety of the run, (2) pulsing ground-to-Rydberg transitions act globally on all atoms at once, (3) pairs of atoms in excited Rydberg states interact with a van der Waals interaction during the entire run, and (4) measurements of ground and Rydberg
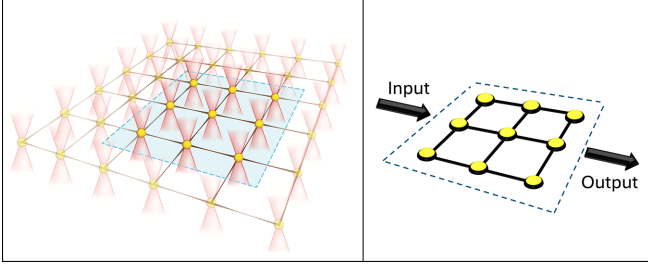
---

*Contact author: scarola@vt.edu

FIG. 1. Left: Schematic of atoms trapped in optical tweezers in an example pattern, a square lattice array. Pairs of atomic hyperfine states within each atom define pseudospins. The lines connecting each atom depict the nearest-neighbor component to the van der Waals interaction. The rectangular dashed line shows a domain as a subset of atoms within the larger array. Right: Schematic of a usable domain abstracted as an ideal graph state. Vertices are spin states $|+\rangle$, and the lines depict entanglement with the CZ gate. The arrows show the information flow in computational order parameters defining domain size.

state populations are recorded globally for all atoms at the end of the run. These analog conditions have the advantage of parallel entanglement using an always-on interaction but exclude many features of digital Rydberg-based devices, e.g., local control of one- and two-atom gates [22,23]. Reference [26] recorded device parameters, local error benchmarks, and other details of the Aquila device.

We test our order parameters on Aquila. Active correction of weak errors would, in principle, imply a uniform finite-size scaling of computational order, and therefore computational domains of arbitrary size. But as error probabilities increase above threshold, we expect a transition to a regime with exponential decay of computational order scaling. To see this, consider one measurement per vertex where the probability of an uncorrelated error in a single measurement at a vertex is ε_M. Nonlocal fidelities derived from n measurements, and therefore computational order, will decrease as $\sim (1 - \varepsilon_M)^n$ as we grow the number of measurements and vertices. We parametrize the error probability in the Aquila device with similar scaling functions for computational order parameters. Our scaling analysis indicates that errors limit domain sizes to be more than an order of magnitude smaller than those needed for thresholds implied by Eq. (1). Our domain-based benchmarks complement other recently implemented neutral atom benchmarking tools [25,27–29].

The paper is organized as follows. Section II discusses the model of atoms in the Aquila device and presents the method to create and characterize graph states. In Sec. II A we discuss the Rydberg atom quantum analog simulator Hamiltonian. Here, we show how the always-on van der Waals interaction between atoms can be used to create graph states using parallel entanglement. We also quantify unitary errors inherent to the always-on protocol. In Sec. II B we discus how to characterize graph states with stabilizer and string correlation functions. In Sec. II C we discuss measurement-based logic operations in the Clifford group as computational order parameters. Section III presents results from the Aquila device. In Sec. III A we create two-particle entangled states on Aquila and test fidelity. In Secs. III B and III C we create graph states

on Aquila and characterize them to estimate computational domain sizes. Section III D discusses error sources. We summarize in Sec. IV.

II. MODEL AND METHODS

A. Hamiltonian and always-on interaction

We define the model and wave function of Rydberg atoms trapped in optical tweezer arrays. Once N atomic locations are fixed in the plane by optical tweezers, the time-dependent Hamiltonian is [23,26]

$$\hat{H}(t) = \hat{H}_0(t) + \hat{V}$$

$$\hat{H}_0(t) = \frac{\Omega(t)}{2} \sum_{i=1}^{N} \left[e^{i\phi(t)} |g_i\rangle\langle r_i| + e^{-i\phi(t)} |r_i\rangle\langle g_i| \right]$$

$$\hat{V} = \sum_{i<j}^{N} V(d_{ij}) |r_i\rangle |r_j\rangle\langle r_j|\langle r_i|,$$

where $|g_i\rangle$ ($|r_i\rangle$) denotes the ground (excited Rydberg) state of the ith atom. The location of each atom defines graph vertices in the real space plane. $V(d_{ij}) = C_6/d_{ij}^6$ are the interatom interaction strengths where, for the Aquila device, $C_6 = 5420503 \, \mu m^6 rad/\mu s$ and d_{ij} is the planar interatom separation. For each graph we use uniform distances, $d_{i,j} = d$, except at certain input vertices discussed in Sec. II C. The Rabi drive amplitude $\Omega(t)$ and the phase $\phi(t)$ can be pulsed during the run. We set $\hbar = 1$.

The atomic states define a pseudospin. $\hat{H}$ can be written in terms of the usual Pauli matrices at atom i, $\hat{\boldsymbol{\sigma}}_i = (\hat{\sigma}_i^x, \hat{\sigma}_i^y, \hat{\sigma}_i^z)$, using $\hat{\sigma}_i^z = 1 - 2|r_i\rangle\langle r_i|$ and $\hat{\sigma}_i^x = |g_i\rangle\langle r_i| + |r_i\rangle\langle g_i|$. The eigenbasis of $\hat{\sigma}_i^x$ is then $|\pm_i\rangle \equiv (|g_i\rangle \pm |r_i\rangle)/\sqrt{2}$. Note that the van der Waals interaction between two atoms evolves as $\exp[-i\hat{V}t]$ to become a controlled-phase operation:

$$\text{CPHASE}_{jk}(\theta) \equiv e^{-i\theta |r_j\rangle |r_k\rangle\langle r_k|\langle r_j|},$$

where $\theta = tV(d_{jk})$ for atoms j and k. This operation becomes a CZ operation between pseudospins at times that are odd multiples of $\pi/V(d_{jk})$, e.g., when we have $\text{CPHASE}_{jk}(\pi)$, as depicted in Fig. 2.

To see the role of an always-on interaction, we construct the wave function in the Schrödinger picture. The exact many-body wave function evolves under the pulse profiles of $\Omega(t)$ and $\phi(t)$ as [26,30]

$$|\psi(t)\rangle = \hat{U}_{\hat{H}_0}(t)\hat{U}_{\hat{V}}(t) \prod_{i=1}^{N} |g_i\rangle \tag{2}$$

$$\hat{U}_{\hat{H}_0}(t) = \mathcal{T} \exp\left[-i \int_0^t \hat{H}_0(\tau)d\tau\right] \tag{3}$$

$$\hat{U}_{\hat{V}}(t) = \mathcal{T} \exp\left[-i \int_0^t \hat{U}_{\hat{H}_0}^\dagger(\tau)\hat{V}(\tau)\hat{U}_{\hat{H}_0}(\tau)d\tau\right], \tag{4}$$

where $\mathcal{T}$ denotes time ordering. For $\hat{V} = 0$, properly designed pulse profiles $\Omega(t)$ and $\phi(t)$ can be used to simultaneously rotate all atoms in pseudospin space. But for $\hat{V} \neq 0$, we must consider the simultaneous evolution of the single-atom control fields along with the interaction, because $\hat{H}_0$ and $\hat{V}$ do not
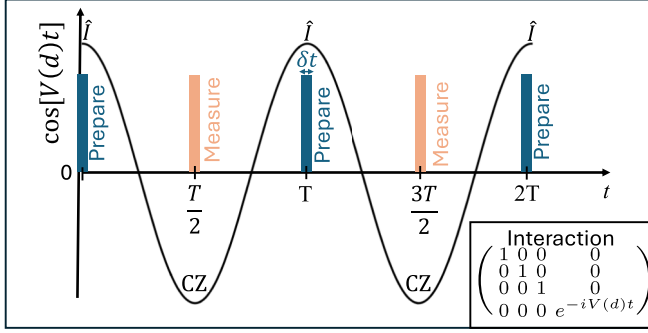
FIG. 2. Schematic of time scales in the always-on interaction protocol for creation of graph states with the controlled phase interaction between atoms. The solid line plots the real part of the phase in the interaction matrix as a function of time. The slow interaction is a controlled phase operation between the atom pairs that approximates the two-spin identity gate $\hat{I}$ at times that are even multiples of $T/2$ and the CZ gate at odd multiples, where $T = 2\pi/V(d)$. The bars are schematics labeling times for short pulsing stages of duration δt. The preparation stage uses a global Rabi-drive pulse to simultaneously rotate all atoms from $|g_i\rangle$ into the state $|+_i\rangle$. The measurement stage similarly rotates all atoms and then measures $\{|g_i\rangle, |r_i\rangle\}$ populations. The inset shows the matrix for two-particle interaction time evolution, $\exp[-i\hat{V}t]$, in the basis $\{|g_1\rangle|g_2\rangle, |g_1\rangle|r_2\rangle, |r_1\rangle|g_2\rangle, |r_1\rangle|r_2\rangle\}$.

commute in general. We will see below that the Schrödinger picture wave function conveniently separates the roles of $\hat{H}_0$ and $\hat{V}$, whereas the separation is harder to see in the more conventional interaction picture wave function, $\hat{U}_{\hat{V}}(t)\prod_{i=1}^{N}|g_i\rangle$.

We now discuss the always-on interaction as a route to create graph state edges with Rydberg atom arrays and estimate the impact of noncommutativity of $\hat{H}_0$ and $\hat{V}$. Figure 2 depicts subsequent rounds of preparation and measurement to create graph states and execute MBQC measurement protocols. Ideally, preparation of $\prod_i |+_i\rangle$ allows the interaction to drive evolution into graph states for times at odd multiple of $T/2$. For infinitely narrow pulses and short-ranged interaction, this protocol leads to ideal graph states and can be efficiently scaled because it uses only global pulses. For example, after the first measurement stage we expect a graph state:

$$\prod_{\langle j,k\rangle \in \mathcal{E}} \mathrm{CPHASE}_{j,k}(\pi) \prod_i |+_i\rangle, \qquad (5)$$

where $\langle j, k\rangle$ indicates atom pairs defining graph edges $\mathcal{E}$. Figures 3(a)–3(d) depict example vertex-edge combinations we build on Aquila.

Perturbations arise due to finite pulse widths and long-range parts of the interaction. These perturbations are known unitaries that can be incorporated into a definition of a weighted graph state [1]. Alternatively, known local unitary errors can be corrected with pulse engineering [31,32] and perturbations due to the long-range interaction can be removed with additional pulsing [33]. Here, we instead take these perturbations to be graph-state preparation errors and quantify their impact.

We quantify the perturbation to the desired graph state caused by nonzero pulse widths evolving along with the interaction. Consider the first preparation stage, $0 \leqslant t \leqslant \delta t$, depicted schematically by the first vertical bar in
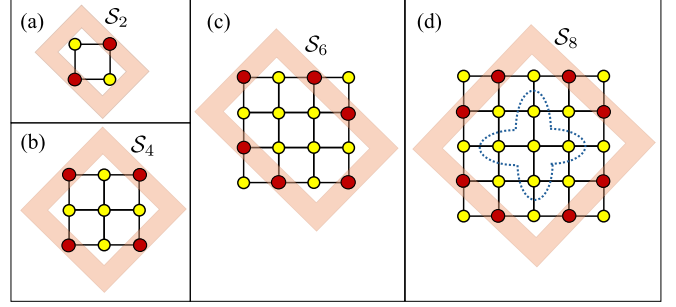

FIG. 3. Schematics of example graph states created on Aquila. Each circle represents an atom prepared in the $|+\rangle$ state. Solid black lines depict entanglement with the always-on interaction approximation to the two-atom CZ operation. The shaded rectangles enclose atoms used to measure example strings $\mathcal{S}_n$ defining nonlocal order parameters, Eq. (8). Atoms covered by $\mathcal{S}_n$ are shaded in red. In (d), the dotted line about the center i_c encloses five atoms defining an example of one stabilizer operator that we measure to find $\langle \hat{S}_{i_c}\rangle$.

Fig. 2. Assume for simplicity that $\hat{H}_0(t)$ is a square pulse during the preparation stage. To create a graph state we seek to first prepare $\prod_i |+_i\rangle$ using just single-atom rotations: $\hat{U}_{\hat{H}_0}(\delta t)\prod_{i=1}^{N}|g_i\rangle$. Ideally, interactions should entangle the state only after single-atom rotations are applied. But, the interaction perturbs the first preparation stage because it is always on. To approximate the role of interactions, consider the first-order Dyson series expansion for the propagator:

$$\hat{U}_{\hat{V}}(\delta t) = \hat{I} - i\int_0^{\delta t} e^{i\hat{H}_0\tau}\hat{V}e^{-i\hat{H}_0\tau}d\tau + O([\delta t V(d)]^2). \quad (6)$$

Substitution into Eq. (2) shows that the second term in Eq. (6) induces a preparation-stage correction (a unitary error) due to the always-on interaction, i.e., it causes deviations from $\hat{U}_{\hat{H}_0}(\delta t)\prod_{i=1}^{N}|g_i\rangle$. Note that the correction to $\hat{I}$ scales as $\delta t V(d)$ in the wave function and therefore vanishes linearly for $\delta t \to 0$. As mentioned above, pulse engineering [31,32,34] can, in principle, push the error to higher order in δt. But, as we will see quantitatively, the linear perturbation has a small effect on Aquila compared to other perturbations because we are able to choose single-atom pulse widths such that $\delta t/T$ is below 0.25 on Aquila. A similar analysis applies to short pulses in the measurement stage for times near $T/2$. We can therefore accurately characterize the weak unitary deviations of $\hat{U}_{\hat{V}}$ from $\hat{I}$ (CZ) during the preparation (measurement) stages. In the remainder of this work we consider only one preparation and one measurement stage.

B. Stabilizer and string correlators in graph states

We now discuss the characterization of graph states as depicted in Figs. 3(a)–3(d) using expectation values of stabilizer and string correlation functions. Measurement-based benchmarking can be implemented by testing the fidelity of local stabilizer operators and nonlocal string correlators defined by stabilizer products. Products of stabilizer operators bound MBQC computational order because MBQC protocols are defined from combinations of stabilizer operator products.

Graph states are eigenstates of stabilizer operators defined by [1]

$$\hat{S}_i = \hat{\sigma}_i^x \prod_{j \in \mathcal{N}} \hat{\sigma}_j^z, \tag{7}$$

where the product runs over the connections to vertices in the neighborhood of i, $j \in \mathcal{N}$, to define graph edges. We may test the stabilizer average given by $N_s^{-1} \sum_{i=1}^{N_s} \hat{S}_i$, where N_s is the number of stabilizer operators fitting within the graph. The dotted line in Fig. 3(d) encircles five vertices defining one example stabilizer operator. Since graph states are unique eigenstates of $\hat{S}_i$ with eigenvalue $+1$, we expect to obtain unity on an ideal graph state. $N_s^{-1} \sum_{i=1}^{N_s} \hat{S}_i$ therefore serves as an example graph-state fidelity measure.

We can also use $\hat{S}_i$ to construct nonlocal string correlators that can be implemented with global pulses and measurements to reveal scaling for bounds of computational order. Ideal graph states are also eigenstates of products of $\hat{S}_i$ defining nonlocal symmetries, e.g., $\prod_{j \in \mathcal{S}_n} \hat{\sigma}_j^x$, where $\mathcal{S}_n$ denotes certain strings of atoms containing n measurements with one measurement per atom in the string. Figure 3 depicts example strings by rectangular loops passing though included atoms. One can show that the eigenvalue of these example string operators is $+1$ for ideal graph states since all basis states contributing amplitude to the many-body wave function preserve parity of the string symmetry.

We define the expectation value of string symmetries as nonlocal order parameters obtained from n measurements:

$$\Theta_n \equiv \left\langle \hat{\mathcal{P}}_{\mathcal{S}_n}^+ \left[\prod_{j \in \mathcal{S}_n} \hat{\sigma}_j^x \right] \hat{\mathcal{P}}_{\mathcal{S}_n}^+ \right\rangle, \tag{8}$$

where $\hat{\mathcal{P}}_{\mathcal{S}_n}^+$ are projectors onto basis states preserving the $+1$ string parity. $\hat{\mathcal{P}}_{\mathcal{S}_n}^+$ defines a post selection protocol to set a normalization consistent with conventional fidelity measures: $\Theta_n = 1$ for an ideal graph state and $\Theta_n = 1/2$ for a product state randomized by errors. We implement the projectors by selecting the measurement outcomes that preserve $+1$ parity. This, without loss of generality, excludes the other half of all possible outcomes, i.e., -1 parity outcomes. For example, in Fig. 3(a), the following string outcomes corresponding to amplitude in the two-spin wave function are kept: $|+\rangle|+\rangle$ and $|-\rangle|-\rangle$. Outcomes corresponding to $|+\rangle|-\rangle$ and $|-\rangle|+\rangle$ are rejected.

We can estimate scaling of Θ_n with n using a classical single-atom error model. Let ε_L be the probability that an error causes a measurement of a single-atom state $|\pm\rangle$ to flip to $|\mp\rangle$ anywhere along the length of $\mathcal{S}_n$. Note that Θ_n only changes with an odd number of flips in the eigenbasis of $\hat{\sigma}^x$. The probability of flipping none or any even number of outcomes along the string follows from a binomial distribution:

$$P_e(n) = \sum_{k=0}^{k_m} \frac{n!}{(2k)!(n-2k)!} \varepsilon_L^{2k} (1-\varepsilon_L)^{n-2k}$$
$$= \frac{1}{2}[1 + (1-2\varepsilon_L)^n], \tag{9}$$

where $k_m = n/2$ [$k_m = (n+1)/2$] for n even [odd]. $P_e(n) = 1$ for $\varepsilon_L = 0$. For $\varepsilon_L > 0$, $P_e(n)$ decays exponentially to $1/2$ as n
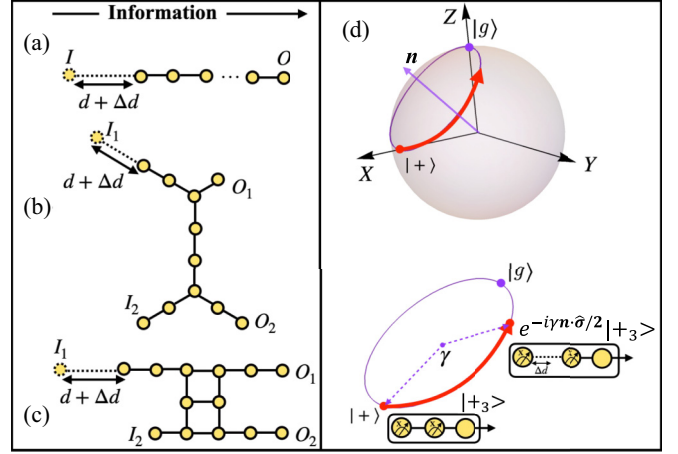

FIG. 4. Measurements on the graphs in (a)–(c) define nonlocal computational order parameters based on MBQC quantum logic operations [18]. (a) Chain graph of atoms where global measurements along the pseudospin-x eigenbasis teleport a quantum state from I to O to execute a logical identity operation. (b) The measurements on this graph take input states at I_1 and I_2 and performs logical controlled-NOT to yield outputs at O_1 and O_2. (c) The same as (b) but for a logical SWAP operation. To prepare input states in (a)–(c), the input atoms are translated by Δd. (d) The red arrow depicts the impact of translation by Δd, measurements, and always-on interaction that takes the input $|+\rangle$ state at I and transforms it so that the third atom is rotated by an angle γ on the Bloch sphere about the unit vector $\mathbf{n} = (1, 0, 1)/\sqrt{2}$. The state at the third atom becomes the input for the rest of the graph.

increases. We take Eq. (9) as an approximate error model for measurements of string correlators of graph states on Aquila that quantifies exponential scaling with a single fitting parameter ε_L.

C. Computational order parameters

We now turn to nonlocal order parameters defined by measurement-based quantum logic operations in the Clifford group. The order parameters rely on global measurements and, by construction, imply the efficacy to compute with the graph state. Since these operations can be scaled in size (larger graphs produce the same logical operation), their fidelities can be used to estimate the scaling with N and n.

We first review the measurement-based protocol to implement a logical identity operation [18,34–36]. Figure 4(a) depicts a chain graph that, upon global measurement, executes logical identity by teleporting the state encoded at input, I (at $i = 1$), to output, O (at $i = N$), where vertices are labeled $i = 1, 2, ..., N$, from left to right. To see this, first consider an ideal chain-graph state with vertices $i = 2, 3, ..., N$:

$$|\psi_c\rangle = \prod_{j=2}^{N-1} \text{CPHASE}_{j,j+1}(\pi) \prod_{i=2}^{N} |+_i\rangle, \tag{10}$$

where we excluded the leftmost vertex at $i = 1$. We then encode information in the leftmost vertex: $|\psi_I\rangle$. Entangling

$|\psi_I\rangle$ with the rest of the graph leads to the state

$$|\psi_e\rangle = \text{CPHASE}_{1,2}(\pi)|\psi_I\rangle|\psi_c\rangle, \tag{11}$$

which is now an N-vertex chain-graph state with encoded information. Measurements on $i = 1, 2, ..., N-1$ move information in $|\psi_I\rangle$ from left to right along the graph. One can show [18] that the output state encodes information at $i = N$ which is, up to a known unitary, the same as the input state:

$$|\psi_O\rangle = \hat{U}_\Sigma \hat{\mathcal{I}}|\psi_I\rangle, \tag{12}$$

where $\hat{\mathcal{I}}$ denotes the logical measurement-based identity operation. $\hat{U}_\Sigma = (\hat{\sigma}^z)^{s_1+s_3+\cdot\cdot}.(\hat{\sigma}^x)^{s_2+s_4+\cdot\cdot}$ is a byproduct unitary that feeds forward measurement outcomes along the chain graph. $s_i = 0, 1$ are the measurement outcomes from a projective x measurement at vertex i.

Equation (12) defines an example measurement-based logical operation in the Clifford group. It implies that ideal graph-state chains allow measurements to teleport information along the chain. Equation (12) arises from the underlying every-other vertex symmetry, $\prod_i \hat{\sigma}^x_{2i+1}$, in one-dimensional graphs and tests a necessary condition for computational power [13]. Also, the expected output in Eq. (12) does not depend on N for an ideal graph state. The fidelity to implement Eq. (12) can therefore be used to benchmark imperfect graph states of any size. Furthermore, only global measurements are needed. Other measurement-based logic operations in the Clifford group can be used to benchmark graph states in a similar fashion. Figures 4(b) and 4(c) depict graphs that, upon global measurement, execute logical controlled-NOT and SWAP operations, respectively, by pushing information from inputs to outputs [18].

It is not possible to directly tune the state of selected input atoms using local fields when operating under the constraints of the Aquila device discussed in Sec. I. We now introduce a method to use graph geometry to effectively tune input states $|\psi_I\rangle$ without local fields. We consider construction of a chain-graph state of atomic pseudospins using the always-on interaction. All atoms are first globally prepared in the $|+\rangle$ state. Entangling atoms $i = 2$ to N with the two-atom CZ operation approximates $|\psi_c\rangle$. But, to encode information at the left side of the chain-graph state we entangle the $|+_1\rangle$ state with a controlled phase operation instead of CZ. To achieve this with the always-on interaction between Rydberg atoms we translate the $i = 1$ atom as depicted in Fig. 4(a). The resulting encoded wave function is

$$|\tilde{\psi}_e\rangle = \text{CPHASE}_{1,2}[TV(d+\Delta d)]|+_1\rangle|\psi_c\rangle. \tag{13}$$

Here, translation by Δd encodes information that can be teleported from the left to the right side of the chain-graph state.

To derive the output state from $|\tilde{\psi}_e\rangle$, consider just the first three atoms: $i = 1, 2, 3$. It is straightforward to show that after using measurement to trace out the first two atoms, the state at $i = 3$ becomes our new input state for the rest of the graph:

$$|\tilde{\psi}_I\rangle = e^{-i\gamma \boldsymbol{n}\cdot\hat{\boldsymbol{\sigma}}/2}|+_3\rangle, \tag{14}$$

i.e., a state rotated about the unit vector $\boldsymbol{n} = (1, 0, 1)/\sqrt{2}$ by an angle γ defined by

$$\tan\left(\frac{\gamma}{2}\right) = \sqrt{2}\tan\left[\frac{T}{2}\{V(d+\Delta d) - V(d)\}\right]. \tag{15}$$

Figure 4(d) depicts the impact of increasing Δd. The remaining measurements along the chain-graph state then teleport $|\tilde{\psi}_I\rangle$ from left to right along the graph to yield the output state

$$|\tilde{\psi}_O\rangle = \hat{U}'_\Sigma\hat{\mathcal{I}}|\tilde{\psi}_I\rangle, \tag{16}$$

where $\hat{U}'_\Sigma$ is a modified byproduct unitary (see Appendix D). Equation (16) shows that the information encoded in the left side of the graph can be teleported to the right side of the graph.

The above protocol combines graph geometry, the always-on interaction, and measurements to program input states. Figures 4(b) and 4(c) depict intentional translation of one input atom for other graphs, where the first three atoms are similarly used to create input states for the rest of the graph. These graphs depict translation of just one atom, but more sophisticated input geometries are possible. In general, our method implies that weighted graph states, instead of local spin rotations, can be used to define input information for unweighted graph states.

We can use the translation operation to build an order parameter with the chain graph in Fig. 4(a). The x measurements of the last (output) atom offer a nonlocal computational order parameter with $n = N$:

$$Q_N(\gamma) = \text{Tr}[\hat{\mathcal{M}}_x\hat{\rho}_O\hat{\mathcal{M}}_x^\dagger], \tag{17}$$

where $\hat{\mathcal{M}}_x$ denotes measurement along the pseudospin x direction of the output atom and $\hat{\rho}_O$ is the density matrix of the output atom. In the ideal case (i.e., in the absence of noise, long-range components to the interaction, and pulse widths) we expect projective x measurements to move the rotated state $|\tilde{\psi}_I\rangle$ to the output atom at O so that $Q_N(\gamma)$ becomes $q(\gamma) \equiv |\langle+|e^{-i\gamma\boldsymbol{n}\cdot\hat{\boldsymbol{\sigma}}/2}|+\rangle|^2 = (3 + \cos[\gamma])/4$. Differences between the device results and the function $q(\gamma)$ serve as nonlocal graph-state benchmarks.

III. IMPLEMENTATION ON AQUILA

A. Two-particle entangled states

We first demonstrate the creation of two-atom superpositions to test the always-on approach. The pulse sequence used to create the state is shown in Appendix A. For $d = 12.3$ μm the pulse sequence and always-on interaction approximates a Bell pair: $|B\rangle = (|g_1\rangle|g_2\rangle + |r_1\rangle|r_2\rangle)/\sqrt{2}$. We find the overlap between $|B\rangle$ and the exact wave function, Eq. (2), to be 0.99, showing that here the correction term discussed in Sec. II A is small.

We also test the implementation of other two-particle entangled states on Aquila. The squares in Fig. 5 plot a fidelity defined as the overlap of the exact wave function, Eq. (2), and the Aquila device. The overlaps demonstrate the high accuracy of the always-on protocol. The error bars are computed using the delete-1 jackknife resampling method to obtain the standard error. We choose enough shots to ensure convergence (Appendix B).

Measurements on the Aquila device have an $\sim$8% measurement bias of the $|r\rangle$ state [26], which we have checked with 1000 single-atom shots. This is the largest source of error. We correct for measurement bias using the stochastic $\mathbb{T}$-matrix method [37–39] described in Appendix C (remaining
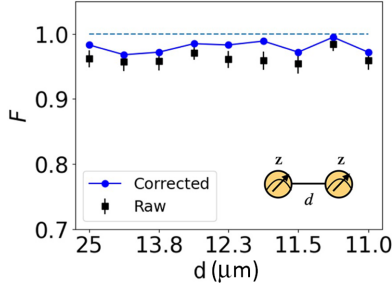
FIG. 5. Fidelity of the two-atom state plotted as a function of interatom distance. Squares plot the overlap of Aquila data with the exact wave function, Eq. (2), using 100 shots. The circles plot the same but for corrected data that account for known [26] measurement bias (see Appendix C). The Bell state is expected at $d = 12.3$ μm. The solid line is a guide to the eye.

sources of error will be discussed in Sec. III D). The circles in Fig. 5 plot the fidelity using measurement-corrected data. We find that the two-particle entangled states are created to within an overlap of ~0.975 after accounting for finite pulse widths and measurement bias.

B. Estimates of stabilizer and string correlators on Aquila

We use Aquila to construct the graph states shown in Fig. 3 and benchmark them using the stabilizer and string correlators. We use the pulse sequence discussed in Appendix A. We first measure the stabilizer sum, $N_s^{-1} \sum_{i=1}^{N_s} \hat{S}_i$, in the pseudospin-$z$ eigenbasis using 1000 shots. For $N = 36$, we find the stabilizer average to be 0.985(6), which is consistent with preparation of a graph state. An average near unity is a necessary but not sufficient demonstration of computational order with graph states. The measurements used here are global and cannot be used with $\hat{S}_i$ to distinguish between graph states and product states (a combination of local x and z measurements are needed [40]). Also, $\hat{S}_i$ is a local (five-atom) operator that does not scale with N or n.

We also used Aquila to infer Θ_n for various strings. The circles in Fig. 6 show how the order parameter decreases with increasing string length. The solid line in Fig. 6 shows a standard fit with Eq. (9) yielding $\varepsilon_L = 0.12(1)$. We have therefore parametrized the exponential decrease in string correlations in these graph states. The threshold $\Theta_n > 1/2$ establishes that fewer than ~9 measurements on nine atoms can be used to distinguish a graph state from a randomized product state. These results therefore provide an upper bound on the domain size across which MBQC can be performed due to errors.

C. Estimates of computational order parameters on Aquila

We now use our protocol to estimate computational order parameters of states engineered on Aquila. We build graph states with various shapes and sizes. To test computational power we benchmark the states with the computational order parameters discussed in Sec. II C.

We first create the chain graph state, Fig. 4(a). While two-qubit fidelities are high, we must benchmark the computational power of the many-body wave function as system size
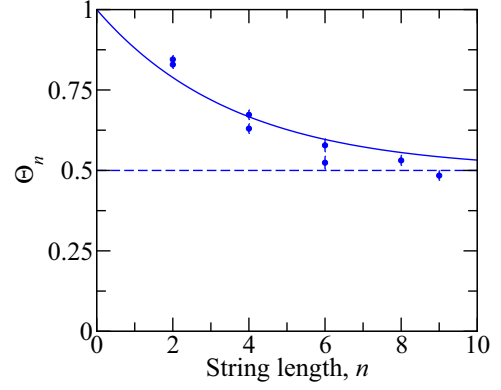

FIG. 6. The circles plot estimates of string order, Eq. (8), as a function of string length taken with 1000 shots on Aquila after creating graph states. The data are corrected for measurement bias (Appendix C). Graphs with up to 36 atoms were used and example strings are plotted in Fig. 3. The solid line shows a single parameter fit using Eq. (9) to find $\varepsilon_L = 0.12(1)$. The horizontal dashed line plots the threshold for a randomized product state.

is scaled. We use $Q_N(\gamma)$ [see Eq. (17)] and compare with the ideal case, $q(\gamma)$.

Figure 7 shows measurement results along with results from numerical simulation and $q(\gamma)$. The horizontal shift between $q(\gamma)$ and the numerical simulation result shows the impact of finite pulse widths. The overall trend in the measurements shows evidence for teleportation of the rotated input state across the entire chain graph.

We now turn to scaling estimates of the teleportation fidelity $Q_N(0)$ with N. We expect $Q_N(0) = 1$ for no error and $Q_N(0) = 1/2$ for large error. As in Sec. II B, we consider an uncorrelated measurement error model to construct a scaling function. We assume that measurement errors change values of s_i in the byproduct operator. Applying a byproduct operator with incorrect s_i to $|\pm_i\rangle$ will only cause an error if s_i is changed an odd number of times on atoms $i = 1, 3, 5, ..., N$, for N odd. We therefore see that an odd number of measurement errors must occur on the $n_O \equiv (N + 1)/2$ atoms (at every other atom) to cause an error, consistent with the every-other-vertex symmetry, $\prod_i \hat{\sigma}_{2i+1}^x$. This motivates a scaling fidelity $P_e(n_O)$ that parametrizes the total probability for only an even number of measurement errors to occur on n_O atoms. Appendix E discusses an alternative scaling function based on amplitude damping in a trajectory model [41].

Teleportation fidelity, and therefore $Q_N(0)$, has a threshold. A teleportation fidelity above 2/3 guarantees teleportation across a quantum channel [34,42–44]. A fidelity below 2/3 leaves no guarantee that the graph contains a quantum channel. We use this threshold to define domain size.

Figure 8 shows the scaling in measurement-based teleportation we obtain from the Aquila device. The triangles show a theoretical expectation for $Q_N(0)$ that incorporate the errors due to the finite pulse width and the long-range part of the interaction using the exact wave function. The squares show the raw data from Aquila and the circles show the data corrected for measurement bias. The solid lines show single parameter fits with $P_e(n_O)$. A standard fit to the
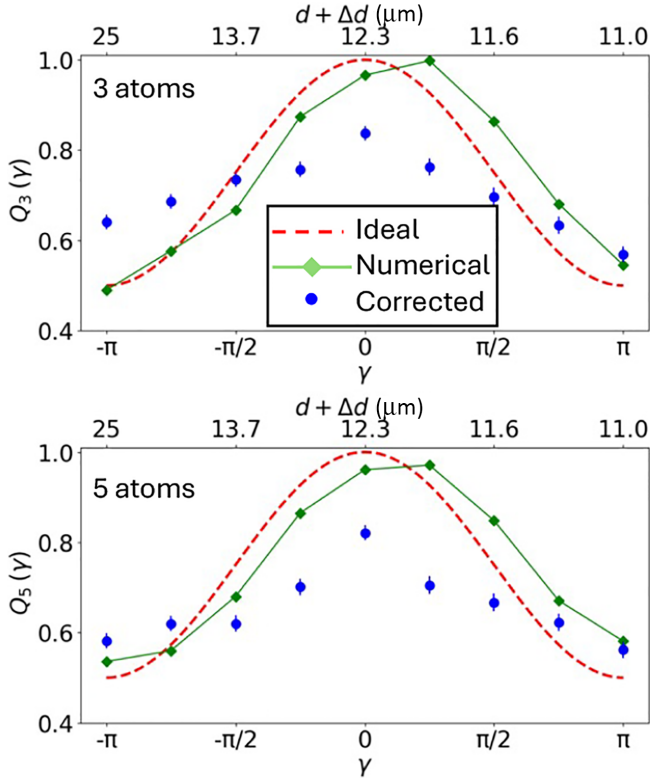
FIG. 7. Example results for teleportation along chain graphs with three and five atoms on the top and bottom, respectively. The x axis is the rotation angle implemented by translating the first atom in the chain graph by Δd [see Figs. 4(a) and 4(d)]. The red dashed line shows the ideal case, $q(\gamma) = (3 + \cos[\gamma])/4$, expected for infinitely narrow pulses, only nearest-neighbor interaction, and no other sources of error. The solid green line shows results from a numerical simulation that includes errors from finite pulse widths. The circles are results from the Aquila device with 1000 shots, corrected for measurement bias (Appendix C).
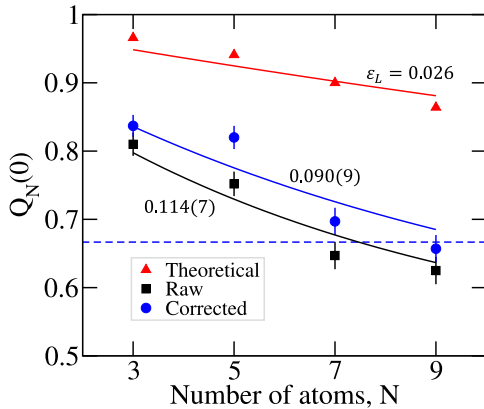

FIG. 8. The teleportation fidelity along the chain graph as a function of the number of atoms. The triangular data points are a theoretical prediction using the exact wave function, Eq. (2), that includes errors due to the finite pulse widths (see Appendix A for the pulse shapes) and long-range parts of the interaction. The squares are raw data from Aquila and the circles plot data corrected for measurement bias. The solid lines are single parameter fits with $P_e(n_O)$ to obtain ε_L. The horizontal dashed line depicts the 2/3 threshold below which we cannot guarantee teleportation along a quantum channel.

corrected data yields $\varepsilon_L = 0.090(9)$, consistent with the string error probability obtained in Sec. II B and the error model in Appendix E. The corrected data fall below 2/3 for chain graphs with $N \gtrsim 9$. This is also consistent with results from Sec. II B showing that string lengths $n \gtrsim 9$ had a saturated string order parameter. We therefore conclude that our implementation of graph states on Aquila support computational domains smaller than ~ 9 atoms and measurements. These domain sizes imply that we can also demonstrate the MBQC controlled-NOT operation. We were able to demonstrate the MBQC controlled-NOT operation [see Fig. 4(b)] to within an accuracy of 68(2)% using 1000 shots after correcting for measurement bias.

Figure 4(c) depicts the minimal graph needed to implement the measurement-based logical SWAP operation where input states are pushed by measurement, from left to right, to eventually swap at the output. The six central vertices in the SWAP operation can be scaled up to rectangular arrays of arbitrary size. This makes the MBQC SWAP operation the perfect candidate order parameter to test two-dimensional domain size scaling. The graph shown in Fig. 4(c) is too large to implement given the current error budget on Aquila.

D. Error budget on Aquila

Several different error sources on Aquila impact the computational order parameters. The scaling estimate of ε_L in Fig. 8 can be thought of as an aggregate parametrization of many error sources. We interpret the accumulation of error using the known hierarchy of errors on Aquila [26]. The largest single source of error is the measurement bias, which we mostly account for by using measurement-corrected Aquila data to find $\varepsilon_L = 0.090(9)$. Error also arises from (unitary) perturbations from the finite pulse width and the long-range part of the interactions. These errors are included in the estimate of error in $\varepsilon_L = 0.026$ in Fig. 8. We conclude that the difference between the corrected and theoretical fits, $\Delta\varepsilon_L = 0.064(9)$, can be understood as due to remaining sources of error.

Fluctuations in positions of the atoms due to thermal motion and tweezer location errors: $\delta d \approx 0.25$ μm [26], are another possible source of error. Modeling the fluctuations as fast harmonic oscillations in each planar direction, the interaction during the pulse experiences an averaged perturbation of $\sim 36 C_6 \delta d / d^7$ which we have checked changes ε_L by less than 0.01. We conclude that atom location errors are not a dominant contributor to $\Delta\varepsilon_L$.

The largest contributions to $\Delta\varepsilon_L$ are most likely due to an accumulation of single-atom decoherence effects. Single-atom decoherence has been characterized by T_2^* Ramsey measurements where it was found [26] that $|g\rangle$-to-$|g\rangle$ transitions driven by conventional Ramsey pulses have an error probability of ~ 0.07 after $t = 2$ μs. (Possible sources include detuning from laser and Doppler effects, as well as the hybridization and decay with the intermediate state [26]). This error probability is consistent with our estimate of $\Delta\varepsilon_L = 0.064(9)$. We therefore conclude that single-atom decoherence effects are the remaining dominant sources of error in our scaling estimate of ε_L.

IV. DISCUSSION AND OUTLOOK

Nonlocal order parameters based on stabilizers and MBQC logic operations in the Clifford group can characterize graph states of any size. These order parameters test the viability of graph-state entanglement and measurements to execute measurement-based logic operations. Finite-size scaling of the order parameters define the error-limited domain size over which graph states can be used for computation provided we define order parameter thresholds. We imposed a threshold to string order to distinguish it from a classical string, $\Theta_n > 1/2$, and a bound for guaranteed teleportation along a quantum channel, $Q_N(0) > 2/3$.

We demonstrated graph-state construction on QuEra's Aquila device. An always-on interaction enables parallel entanglement. Two types of unitary perturbations cause deviations from ideal graph states. First, the noncommutativity of Rabi-drive pulses and the van der Waals interaction leads to unitary perturbations quantified with a Dyson series expansion. Second, long-range components to the interaction also lead to perturbations. We interpreted these quantifiable perturbations as state preparation errors. They are relatively small and can be corrected with pulse engineering using modified control fields, e.g., refocusing schemes [31,32,34] and Floquet methods [33]. Alternatively, these intrinsic perturbations can be kept as useful [4] features in defining weighted graph states [1].

Scaling of computational order parameters tested the accumulation of errors. Unitary errors arose from the always-on approach. Other error sources included measurement errors and single-atom decoherence effects. The ideal operating regime for the always-on approach is one where T is much longer than pulse durations but much shorter than decoherence times. We found that errors limit computational order to domains containing fewer than ~ 9 measurements on as many atoms on Aquila using both the string order and the teleportation thresholds to define domain size. Errors therefore limit the graph state domain size for MBQC to be less than nine vertices.

We can compare the domain sizes found here with an ideal case. Assuming only measurement errors such that $\epsilon_M \ll 1$, we set $P_e(n_O)$ to 2/3 to find domain sizes of $\sim \ln[3]/\epsilon_M$ vertices. The error probability threshold given by Eq. (1) thus leads to domains of 145 vertices. Computational domains of at least 145 vertices must therefore be embedded inside larger graph states to correct measurement errors. We therefore conclude that domains size found on Aquila are more than an order of magnitude smaller than the minimum needed to implement active error correction on a graph state.

Quantum graph states are ideally constructed from parallel application of entangling gates. We showed that Aquila allows parallel entangling gates using the always-on Rydberg interaction. But this analog mode of operating currently has limited coherence. Significant improvements in scaling of computational order can be obtained by implementing high-accuracy features of neutral atom digital quantum computing, e.g., rapid or high-fidelity measurements implemented in optical lattices [45] and those demonstrated in recent Rydberg atom tweezer arrays [22–25,27,28,46–59].
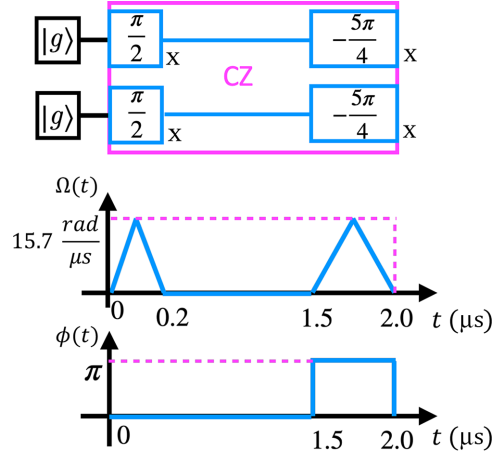

FIG. 9. Pulse sequence used to create two-particle entangled states. Atoms begin in $|g\rangle$. In the absence of interaction or other perturbations, the ideal preparation (measurement) stage rotates both atoms around the pseudospin x axis by $\pi/2$ ($-5\pi/4$). The always-on interaction perturbs the otherwise ideal pulses. The interaction eventually approximates the CZ operation after 2 μs. Measurements are performed at the end. For these parameters, the final state approximates a Bell pair state $|B\rangle$ when atoms are separated by $d = 12.3$ μm.

ACKNOWLEDGMENTS

APPENDIX A: PULSE PROFILES

This section presents the pulse profiles used to create quantum states on the Aquila device. Figure 9 shows the circuit used to construct two-atom Bell pairs with the always-on interaction. The preparation stage is in the first 0.2 μs and the measurement stage is in the last 0.5 μs. Several pulse shapes were tested. Triangular pulse shapes for $\Omega(t)$ yielded the highest fidelity under the constraint of narrow pulse widths.

Figure 10 shows the pulse sequence to create chain graph states. Here, the always-on interaction simultaneously entangles all atoms. The preparation stage is in the first 0.2 μs and the measurement stage is in the last 0.2 μs. All other graph states are created with this pulse sequence as well.

APPENDIX B: ERROR BARS AND SHOT NUMBER

This section describes how the shot number on Aquila was selected. The number of shots required to achieve sufficiently small error bars increases with n. The two-atom data presented in Fig. 5 required only 100 shots to achieve convergence within tolerances set by small error bars, but for larger graphs we increased the shot number.

Figure 11 shows an example convergence check for data taken on Aquila with $N = 5$ and $n = 5$ using the pulse profile from Appendix A. Here, we see no statistically significant deviation for large numbers of shots and that 1000 shots are
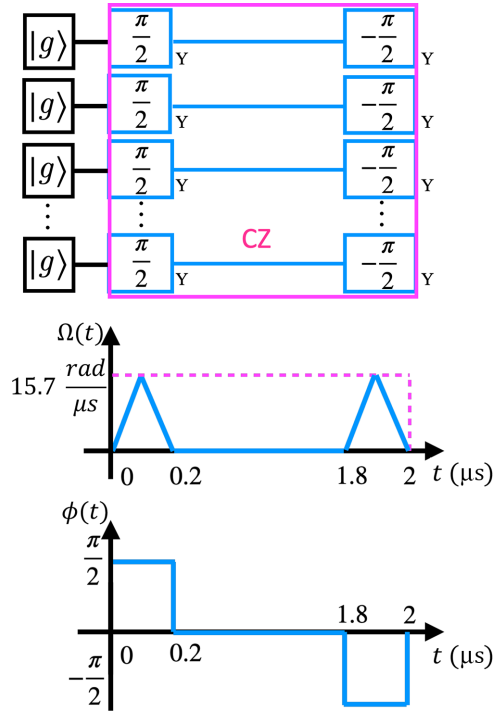
FIG. 10. The pulse sequence used to create graph states where the preparation (measurement) stage rotates all atoms around the pseudospin-y axis by $\pi/2$ $(-\pi/2)$. The always-on interaction approximates the CZ operation between nearest neighbors with $d = 12.3\,\mu\text{m}$ in the graph after 2 μs. Measurements are performed at the end.

more than sufficient for convergence to within small error bars. The main text presents averages using enough shots to ensure convergence.
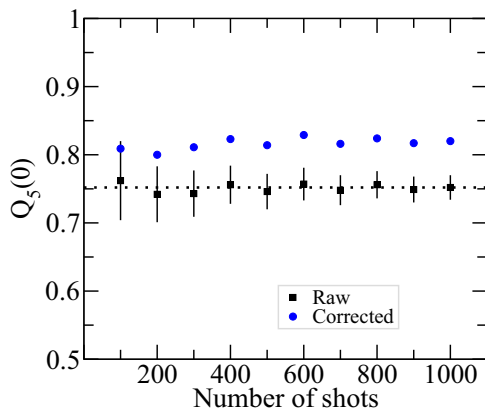

FIG. 11. An example convergence check plotting the estimate of $Q_5(0)$ [see Eq. (17)] obtained from Aquila (squares) as a function of the number of shots used in computing averages. The horizontal dotted line shows the average of raw data obtained with 1000 shots, 0.752, used in the main text. The circles plot the measurement corrected averages. The error bars for the corrected data are very close to the error bars shown for the raw data and have been omitted for clarity.
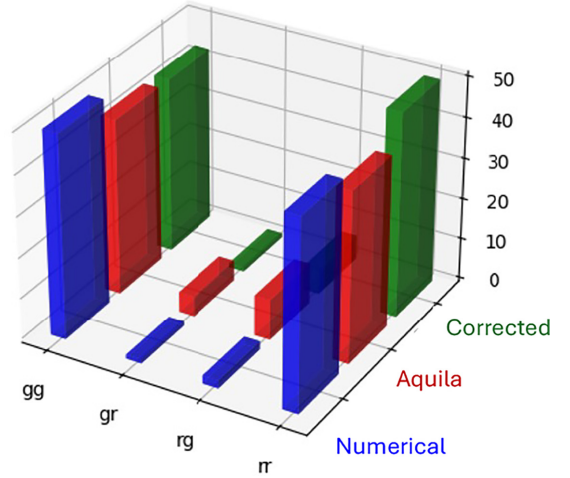

FIG. 12. Example data for two atoms prepared to create a Bell state using the always-on interaction with the pulse protocol discussed in Appendix A with 100 shots and $d = 12.3\,\mu\text{m}$. The histograms plot the number of outcomes. The corrected data plot $\boldsymbol{m}_{\text{corr}}$ and show an improvement over the raw data from Aquila. The numerical simulation includes corrections due to the finite pulse width during the always-on interaction.

APPENDIX C: MITIGATION OF MEASUREMENT BIAS

This section describes an error mitigation protocol for uncorrelated classical measurement error. In this section we assume $n = N$. On the Aquila processor, the largest error source is a measurement bias where a fraction $\epsilon_M \approx 0.08$ of measurements of the state $|g\rangle$ are incorrect and should be $|r\rangle$ [26]. We correct these measurement errors using the $\mathbb{T}$-matrix method [37–39]. The left-stochastic error matrix $\mathbb{T}$ maps ideal measurements of $|g\rangle$ and $|r\rangle$ to noisy output via $\boldsymbol{m}_{\text{meas}} = \mathbb{T}\boldsymbol{m}_{\text{corr}}$, where $\boldsymbol{m}_{\text{corr}}$ and $\boldsymbol{m}_{\text{meas}}$ are vectors containing normalized measurement counts for each outcome for the corrected and measured set, respectively. By inverting this matrix, we correct measured data to account for measurement bias using $\boldsymbol{m}_{\text{corr}} = \mathbb{T}^{-1}\boldsymbol{m}_{\text{meas}}$. Data labeled "corrected" plot results using $\boldsymbol{m}_{\text{corr}}$.

For uncorrelated classical measurement error, the single-atom error generalizes to N-atom error. For a single atom at $i = 1$, $\boldsymbol{m}_{\text{meas}}$ has two entries: the number of counts for outcomes $|g\rangle$ and $|r\rangle$. For one atom, the correction matrix has 2×2 elements and is given by

$$\mathbb{T}_1 \equiv \begin{bmatrix} 1 & \epsilon_M \\ 0 & 1 - \epsilon_M \end{bmatrix}. \tag{C1}$$

For n independent measurements (one per atom) on atoms $i = 1, ..., N$, $\mathbb{T}$ has $2^n \times 2^n$ elements given by the tensor product of single-atom matrices. $\mathbb{T}$ is the matrix used to correct measurement bias discussed in the main text. Figures 12 and 13 show improvements in example outcomes.

APPENDIX D: PROTOCOL FOR POSTPROCESSING MEASUREMENTS

The graphs depicted in Figs. 4(a)–4(c) yield outputs that are the results of logic operations on input states after mea-

TABLE I. Protocol for processing measurements in the first three atoms in a chain graph where the first atom is intentionally translated by Δd (see Fig. 4). The first column lists the four possible outcomes of measurements in the pseudospin eigenbasis of $\hat{\sigma}^x$ of the first two atoms. The second column lists the unitary that impacts the third atom due to the projective measurements on atoms 1 and 2. The third column shows what data to discard so that the pseudospin state of the third atom is rotated by an angle γ on the Bloch sphere.

Outcome	Operation	Choice
10	$\hat{I}$	Discard
11	$\hat{I}$	Discard
01	$\exp[-i\gamma\boldsymbol{n}\cdot\hat{\boldsymbol{\sigma}}/2]$	Keep
00	$\exp[-i\gamma\boldsymbol{n}\cdot\hat{\boldsymbol{\sigma}}/2]$	Keep

surements in the pseudospin eigenbasis of $\hat{\sigma}^x$. A feed-forward of the measurement results of each atom is needed to interpret the output(s). The output of measurements for each atom is recorded and used offline in a byproduct unitary applied to the state(s) measured at the output(s). These byproduct operators are derived for cluster states in Ref. [18]. For the identity operation in the chain graph [$\Delta d = 0$ in Fig. 4(a)] the byproduct unitary is $\hat{U}_\Sigma = (\hat{\sigma}^z)^{s_1+s_3+\cdots}(\hat{\sigma}^x)^{s_2+s_4+\cdots}$, where $s_i = 0, 1$ are the measurement outcomes of the ith atom. The following discusses the protocol defining $\hat{U}'_\Sigma$ in Eq. (16).

To rotate the input state using distorted graphs with $\Delta d \neq 0$ [Fig. 4(d)], we must construct a new feed-forward protocol for $\hat{U}'_\Sigma$. Consider three atoms where the first is a distance $d + \Delta d$ from the second but atoms 2 and 3 are separated by d such that the interaction pulse time approximates a CZ gate between atoms 2 and 3. Measuring atoms 1 and 2 in the eigenbasis of $\hat{\sigma}^x$ leads to four possible outcomes, listed in the first column of Table I. By starting with the eigenstate corresponding to the three-atom perturbed graph state it is straightforward to show that a partial trace of the projective measurements performed on the first two atoms leads to a
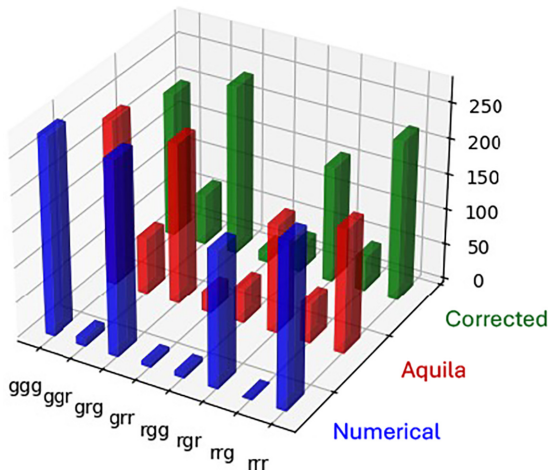

FIG. 13. The same as Fig. 12 but for the three-atom chain-graph state using the pulse sequence shown in Fig. 10 with 1000 shots.
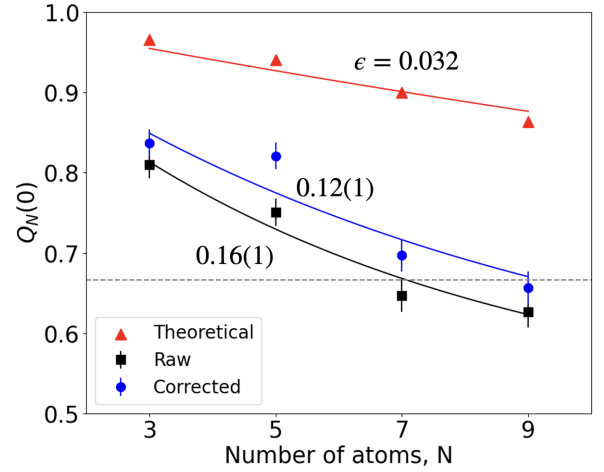

FIG. 14. The symbols plot the same as Fig. 8. The solid lines are single parameter fits with Eq. (E1) to obtain ϵ.

rotated output state at atom 3 only if outcomes 01 or 00 are obtained on the first two atoms. Outcomes 10 and 11 have no impact. The second column in Table I lists the effective operation enacted on $|+_3\rangle$ by the measurement process. The data shown in Fig. 7 only shows results where the first two atoms have outcomes 01 or 00. This choice has the effect of rotating the state of the third atom for use as an input state to the remaining part of the graph, where we then use the conventional cluster state byproduct operators, $(\hat{\sigma}^z)^{s_3+s_5+\cdots}(\hat{\sigma}^x)^{s_4+s_6+\cdots}$, for postprocessing.

APPENDIX E: TRAJECTORY MODEL FOR TELEPORTATION FIDELITY SCALING

In this section we consider an alternative fidelity model to fit teleportation scaling data discussed in Sec. III C. We rely on a quantum trajectory model [41] to study the impact of noise on the scaling of fidelity of the quantum state teleported along the chain graph. We define the fidelity F_N as the overlap of the initial state with the output state. As measurements move the initial state along the chain graph, noise perturbs the state. Each step can be modeled as a move along a trajectory randomized by noise. The resulting teleportation fidelity along an N atom chain graph, assuming amplitude damping noise, is given by [41]

$$F_N = \tfrac{1}{2}(1 + e^{-\epsilon N}), \tag{E1}$$

where ϵ is the probability that the state of a single atom decays. Note that for $\epsilon = \epsilon_L$, F_N and $P_e(N/2)$ both become $1 - \epsilon N/2 + O(\epsilon^2)$ for low error probability.

Figure 14 plots the same as Fig. 8 but using a standard fit with Eq. (E1). Here, we see that the extracted error probability for the corrected data, $\epsilon = 0.12(1)$, is near the value shown in Fig. 8, $\epsilon_L = 0.090(9)$. The comparison in this section shows that exponential decay fidelities based on either dominate measurement errors or amplitude damping errors yield similar scaling parametrizations.

[1] M. Hein, W. Dür, J. Eisert, R. Raussendorf, M. Van den Nest, and H.-J. Briegel, in *Proceedings of the International School of Physics "Enrico Fermi"*, Quantum Computers, Algorithms and Chaos, Vol. 162 (IOS Press, 2006), pp. 115–218.

[2] M. Gachechiladze, C. Budroni, and O. Gühne, Extreme violation of local realism in quantum hypergraph states, Phys. Rev. Lett. **116**, 070401 (2016).

[3] N. Shettell and D. Markham, Graph states as a resource for quantum metrology, Phys. Rev. Lett. **124**, 110502 (2020).

[4] S. Anders, M. B. Plenio, W. Dür, F. Verstraete, and H.-J. Briegel, Ground-state approximation for strongly interacting spin systems in arbitrary spatial dimension, Phys. Rev. Lett. **97**, 107206 (2006).

[5] W. Son, L. Amico, and V. Vedral, Topological order in 1D cluster state protected by symmetry, Quantum Inf. Process. **11**, 1961 (2012).

[6] D. V. Else, I. Schwarz, S. D. Bartlett, and A. C. Doherty, Symmetry-protected phases for measurement-based quantum computation, Phys. Rev. Lett. **108**, 240505 (2012).

[7] J. Miller and A. Miyake, Resource quality of a symmetry-protected topologically ordered phase for quantum computation, Phys. Rev. Lett. **114**, 120506 (2015).

[8] T. Devakul and D. J. Williamson, Universal quantum computation using fractal symmetry-protected cluster phases, Phys. Rev. A **98**, 022332 (2018).

[9] D. T. Stephen, H. P. Nautrup, J. Bermejo-Vega, J. Eisert, and R. Raussendorf, Subsystem symmetries, quantum cellular automata, and computational phases of quantum matter, Quantum **3**, 142 (2019).

[10] R. Raussendorf, C. Okay, D.-S. Wang, D. T. Stephen, and H. P. Nautrup, Computationally universal phase of quantum matter, Phys. Rev. Lett. **122**, 090501 (2019).

[11] A. K. Daniel, R. N. Alexander, and A. Miyake, Computational universality of symmetry-protected topologically ordered cluster phases on 2D Archimedean lattices, Quantum **4**, 228 (2020).

[12] D. Azses, R. Haenel, Y. Naveh, R. Raussendorf, E. Sela, and E. G. Dalla Torre, Identification of symmetry-protected topological states on noisy quantum computers, Phys. Rev. Lett. **125**, 120502 (2020).

[13] R. Raussendorf, W. Yang, and A. Adhikary, Measurement-based quantum computation in finite one-dimensional systems: String order implies computational power, Quantum **7**, 1215 (2023).

[14] T. Senthil, Symmetry-protected topological phases of quantum matter, Annu. Rev. Condens. Matter Phys. **6**, 299 (2015).

[15] P. Liao and D. L. Feder, Graph-state representation of the toric code, Phys. Rev. A **104**, 012432 (2021).

[16] P. Liao, B. C. Sanders, and D. L. Feder, Topological graph states and quantum error-correction codes, Phys. Rev. A **105**, 042418 (2022).

[17] R. Raussendorf and H. J. Briegel, A one-way quantum computer, Phys. Rev. Lett. **86**, 5188 (2001).

[18] R. Raussendorf, D. E. Browne, and H. J. Briegel, Measurement-based quantum computation on cluster states, Phys. Rev. A **68**, 022312 (2003).

[19] H. J. Briegel, D. E. Browne, W. Dür, R. Raussendorf, and M. Van den Nest, Measurement-based quantum computation, Nat. Phys. **5**, 19 (2009).

[20] W.-R. Lee, Z. Qin, R. Raussendorf, E. Sela, and V. W. Scarola, Measurement-based time evolution for quantum simulation of fermionic systems, Phys. Rev. Res. **4**, L032013 (2022).

[21] R. Raussendorf and J. Harrington, Fault-tolerant quantum computation with high threshold in two dimensions, Phys. Rev. Lett. **98**, 190504 (2007).

[22] M. Saffman, T. G. Walker, and K. Mølmer, Quantum information with Rydberg atoms, Rev. Mod. Phys. **82**, 2313 (2010).

[23] A. Browaeys and T. Lahaye, Many-body physics with individually controlled Rydberg atoms, Nat. Phys. **16**, 132 (2020).

[24] H. J. Manetsch, G. Nomura, E. Bataille, K. H. Leung, X. Lv, and M. Endres, A tweezer array with 6100 highly coherent atomic qubits, arXiv:2403.12021.

[25] D. Bluvstein, H. Levine, G. Semeghini, T. T. Wang, S. Ebadi, M. Kalinowski, A. Keesling, N. Maskara, H. Pichler, M. Greiner, V. Vuletić, and M. D. Lukin, A quantum processor based on coherent transport of entangled atom arrays, Nature (London) **604**, 451 (2022).

[26] J. Wurtz, A. Bylinskii, B. Braverman, J. Amato-Grill, S. H. Cantu, F. Huber, A. Lukin, F. Liu, P. Weinberg, J. Long, S.-T. Wang, N. Gemelke, and A. Keesling, Aquila: Quera's 256-qubit neutral-atom quantum computer, arXiv:2306.11727.

[27] B. Nikolov, E. Diamond-Hitchcock, J. Bass, N. L. R. Spong, and J. D. Pritchard, Randomized benchmarking using nondestructive readout in a two-dimensional atom array, Phys. Rev. Lett. **131**, 030602 (2023).

[28] A. L. Shaw, Z. Chen, J. Choi, D. K. Mark, P. Scholl, R. Finkelstein, A. Elben, S. Choi, and M. Endres, Benchmarking highly entangled states on a 60-atom analogue quantum simulator, Nature (London) **628**, 71 (2024).

[29] M. Kornjača, H.-Y. Hu, C. Zhao, J. Wurtz, P. Weinberg, M. Hamdan, A. Zhdanov, S. H. Cantu, H. Zhou, R. A. Bravo *et al.*, Large-scale quantum reservoir learning with an analog quantum computer, arXiv:2407.02553.

[30] A. L. Fetter and J. D. Walecka, *Quantum Theory of Many-Particle Systems* (Dover Publications, Newburyport, 2012).

[31] J. A. Jones, Robust Ising gates for practical quantum computation, Phys. Rev. A **67**, 012317 (2003).

[32] L. M. K. Vandersypen and I. L. Chuang, NMR techniques for quantum control and computation, Rev. Mod. Phys. **76**, 1037 (2005).

[33] T. E. Lee, Floquet engineering from long-range to short-range interactions, Phys. Rev. A **94**, 040701(R) (2016).

[34] Z. Qin, W.-R. Lee, B. DeMarco, B. Gadway, S. Kotochigova, and V. W. Scarola, Quantifying entanglement in cluster states built with error-prone interactions, Phys. Rev. Res. **3**, 043118 (2021).

[35] M. S. Tame, M. Paternostro, M. S. Kim, and V. Vedral, Quantum-information processing with noisy cluster states, Phys. Rev. A **72**, 012319 (2005).

[36] Z. Qin, D. Azses, E. Sela, R. Raussendorf, and V. W. Scarola, Redundant string symmetry-based error correction: Demonstrations on quantum devices, Phys. Rev. A **110**, 012465 (2024).

[37] F. B. Maciejewski, Z. Zimborás, and M. Oszmaniec, Mitigation of readout noise in near-term quantum devices by classical post-processing based on detector tomography, Quantum **4**, 257 (2020).

[38] M. R. Geller, Rigorous measurement error correction, Quantum Sci. Technol. **5**, 03LT01 (2020).

[39] Z. Cai, R. Babbush, S. C. Benjamin, S. Endo, W. J. Huggins, Y. Li, J. R. McClean, and T. E. O'Brien, Quantum error mitigation, Rev. Mod. Phys. **95**, 045005 (2023).

[40] S. Jandura and G. Pupillo, Surface code stabilizer measurements for Rydberg atoms, arXiv:2405.16621.

[41] G. G. Carlo, G. Benenti, G. Casati, and C. Mejía-Monasterio, Simulating noisy quantum protocols with quantum trajectories, Phys. Rev. A **69**, 062317 (2004).

[42] M. Horodecki, P. Horodecki, and R. Horodecki, General teleportation channel, singlet fraction, and quasidistillation, Phys. Rev. A **60**, 1888 (1999).

[43] S. L. Braunstein, C. A. Fuchs, H. J. Kimble, and P. van Loock, Quantum versus classical domains for teleportation with continuous variables, Phys. Rev. A **64**, 022321 (2001).

[44] S. Bose, Quantum communication through an unmodulated spin chain, Phys. Rev. Lett. **91**, 207901 (2003).

[45] Y. Wang, X. Zhang, T. A. Corcovilos, A. Kumar, and D. S. Weiss, Coherent addressing of individual neutral atoms in a 3D optical lattice, Phys. Rev. Lett. **115**, 043003 (2015).

[46] H. Labuhn, D. Barredo, S. Ravets, S. De Léséleuc, T. Macrì, T. Lahaye, and A. Browaeys, Tunable two-dimensional arrays of single Rydberg atoms for realizing quantum Ising models, Nature (London) **534**, 667 (2016).

[47] S. Ebadi, T. T. Wang, H. Levine, A. Keesling, G. Semeghini, A. Omran, D. Bluvstein, R. Samajdar, H. Pichler, W. W. Ho, S. Choi, S. Sachdev, M. Greiner, V. Vuletić, and M. D. Lukin, Quantum phases of matter on a 256-atom programmable quantum simulator, Nature (London) **595**, 227 (2021).

[48] P. Scholl, M. Schuler, H. J. Williams, A. A. Eberharter, D. Barredo, K.-N. Schymik, V. Lienhard, L.-P. Henry, T. C. Lang, T. Lahaye, A. M. Läuchli, and A. Browaeys, Quantum simulation of 2D antiferromagnets with hundreds of Rydberg atoms, Nature (London) **595**, 233 (2021).

[49] I. Cong, H. Levine, A. Keesling, D. Bluvstein, S.-T. Wang, and M. D. Lukin, Hardware-efficient, fault-tolerant quantum computation with Rydberg atoms, Phys. Rev. X **12**, 021049 (2022).

[50] E. Deist, Y.-H. Lu, J. Ho, M. K. Pasha, J. Zeiher, Z. Yan, and D. M. Stamper-Kurn, Mid-circuit cavity measurement in a neutral atom array, Phys. Rev. Lett. **129**, 203602 (2022).

[51] T. M. Graham, Y. Song, J. Scott, C. Poole, L. Phuttitarn, K. Jooya, P. Eichler, X. Jiang, A. Marra, B. Grinkemeyer *et al.*, Multi-qubit entanglement and algorithms on a neutral-atom quantum computer, Nature (London) **604**, 457 (2022).

[52] J. W. Lis, A. Senoo, W. F. McGrew, F. Rönchen, A. Jenkins, and A. M. Kaufman, Midcircuit operations using the omg architecture in neutral atom arrays, Phys. Rev. X **13**, 041035 (2023).

[53] S. Ma, G. Liu, P. Peng, B. Zhang, S. Jandura, J. Claes, A. P. Burgers, G. Pupillo, S. Puri, and J. D. Thompson, High-fidelity gates and mid-circuit erasure conversion in an atomic qubit, Nature (London) **622**, 279 (2023).

[54] K. Singh, C. E. Bradley, S. Anand, V. Ramesh, R. White, and H. Bernien, Mid-circuit correction of correlated phase errors using an array of spectator qubits, Science **380**, 1265 (2023).

[55] M. A. Norcia, W. B. Cairncross, K. Barnes, P. Battaglino, A. Brown, M. O. Brown, K. Cassella, C.-A. Chen, R. Coxe, D. Crow *et al.*, Midcircuit qubit measurement and rearrangement in a ^{171}Yb atomic array, Phys. Rev. X **13**, 041034 (2023).

[56] S. J. Evered, D. Bluvstein, M. Kalinowski, S. Ebadi, T. Manovitz, H. Zhou, S. H. Li, A. A. Geim, T. T. Wang, N. Maskara, H. Levine, G. Semeghini, M. Greiner, V. Vuletić, and M. D. Lukin, High-fidelity parallel entangling gates on a neutral-atom quantum computer, Nature (London) **622**, 268 (2023).

[57] D. Bluvstein, S. J. Evered, A. A. Geim, S. H. Li, H. Zhou, T. Manovitz, S. Ebadi, M. Cain, M. Kalinowski, D. Hangleiter *et al.*, Logical quantum processor based on reconfigurable atom arrays, Nature (London) **626**, 58 (2024).

[58] F. Gyger, M. Ammenwerth, R. Tao, H. Timme, S. Snigirev, I. Bloch, and J. Zeiher, Continuous operation of large-scale atom arrays in optical lattices, Phys. Rev. Res. **6**, 033104 (2024).

[59] M. A. Norcia, H. Kim, W. B. Cairncross, M. Stone, A. Ryou, M. Jaffe, M. O. Brown, K. Barnes, P. Battaglino, T. C. Bohdanowicz *et al.*, Iterative assembly of ^{171}Yb atom arrays with cavity-enhanced optical lattices, PRX Quantum **5**, 030316 (2024).